Materials Today Energy 41 (2024) 101521

Contents lists available at ScienceDirect

Materials Today Energy

journal homepage: www.journals.elsevier.com/materials-today-energy/

Spatial configuration of interlayer maximizing suppression and conversion efficiency of lithium polysulfides for advanced lithium−sulfur batteries

Wenxi Wang [a, f], Lubao Liang [b, f], Lintong Gao [b], Qi Cao [b, **], Bo Jing [b], Xianyou Wang [b], Hongshuai Hou [c], Wenli Zhang [d, ***], Yan Lu [a, e, *]

[a] Department for Electrochemical Energy Storage, Helmholtz-Zentrum Berlin für Materialien und Energie, Hahn-Meitner-Platz 1, Berlin 14109, Germany
[b] Key Laboratory of Environmentally Friendly Chemistry and Applications of Ministry of Education, National Base for International Science & Technology Cooperation, National Local Joint Engineering Laboratory for Key Materials of New Energy Storage Battery, School of Chemistry, Xiangtan University, Xiangtan 411105, China
[c] College of Chemistry and Chemical Engineering, Central South University, Changsha, Hunan Province 410083, China
[d] Guangdong Provincial Key Laboratory of Plant Resources Biorefinery, School of Chemical Engineering and Light Industry, Guangdong University of Technology (GDUT), 100 Waihuan Xi Road, Panyu District, Guangzhou 510006, China
[e] Institute for Technical and Environmental Chemistry Friedrich-Schiller-Universität Jena & Helmholtz Institute for Polymers in Energy Applications (HIPOLE) Philosophenweg 7b, Jena 07743, Germany

ARTICLE INFO

Article history:
Received 24 November 2023
Received in revised form
25 January 2024
Accepted 31 January 2024
Available online 3 February 2024

Keywords:
Polyacrylonitrile
Interlayer
Polysulfides
Lithium-sulfur batteries

ABSTRACT

Shuttle effect of polysulfides and sluggish redox kinetics of sulfur are two tricky problems in lithium −sulfur (Li−S) batteries. Engineering interlayer between sulfur cathode and separator is an innovative approach to alleviate these weaknesses. From the spatial perspective, we validate an efficient interlayer by regulating the stacking configuration composed of a conductive layer (carbonized polyacrylonitrile-carbon nanotube, CPCNT) and catalytic layer (carbonized polyacrylonitrile-selenium, CPSe), forming a hierarchical polysulfide suppression and conversion system. Electrochemical measurements reveal that the contact priority of CPCNT or CPSe on sulfur cathode poses a momentous impact on the overall working efficiency of interlayer. Accordingly, CPSe@CPCNT|S enables Li−S batteries to deliver a specific capacity of up to 760 mAh/g at 1.0C after 500 cycles. Impressively, Li−S batteries endure 250 cycles with 87% capacity retention at 0.2C, even under a sulfur loading of 6.1 mg/cm^2. The polysulfide diffusion visualization coupled with finite elemental analyses disclose that CPSe@CPCNT|S configuration shapes a higher diffusion damping towards polysulfides, while maintaining a smooth electron motion pathway from cathode to interlayer for polysulfide conversion, which is the decisive cause of the enhanced electrochemical performance. This research affords a spatial strategy for interlayer design in Li−S batteries and other alkali metal-sulfur batteries.

1. Introduction

Lithium-sulfur (Li−S) batteries are considered as particularly competitive techniques for next-generation energy storage systems, due to their high specific energy density (2600 Wh/kg) and cost-effectiveness [1–3]. However, Li−S batteries remain plagued by multiple fundamental drawbacks even after decades of research and development [4]. One major issue is that the dissolution of polysulfide intermediates (i.e. Li_2S_x, $4 \leq x \leq 8$) induces the notorious 'shuttle effect' during the discharge process [5], leading to the severe loss of active material and rapid capacity fading. Moreover, the intrinsic insulation properties of sulfur and discharge products (e.g. Li_2S or Li_2S_2) also impede the efficient electron transport from the current collector [6], which results in sluggish redox kinetics and poor rate capability of Li−S batteries.

To address these challenges, the research community has innovatively proposed interlayer engineering strategy. Interlayers,

* Corresponding author.
** Corresponding author.
*** Corresponding author.
E-mail addresses: wjcaoqi@163.com (Q. Cao), wlzhang@gdut.edu.cn (W. Zhang), yan.lu@helmholtz-berlin.de (Y. Lu).
[f] These authors contributed equally.

https://doi.org/10.1016/j.mtener.2024.101521

serving as the 'polysulfide warehouse' and 'auxiliary electrode' [7,8], can physically and chemically trap dissolved polysulfides and electrochemically catalyze the redox conversion of active materials, thereby stabilizing the cycling performance and elevate the rate capability of Li−S batteries. Since the seminal work on interlayers (i.e. microporous carbon and conductive multiwalled carbon nanotube) reported by Manthiram's group in 2012 [9,10], numerous materials (e.g. carbon-based [11−13], metal-based [14−17], polymer-based materials [5,7,18] et al.) have been proposed as interlayers in Li−S batteries. To date, the predominant focus of interlayer research is on elaborately designing or modifying the physical/chemical nature of materials [19−21], involving heteroatom doping in graphene [22,23], integration of metal compounds and carbon material [24−28], nanostructure design [29−31], and dimensional regulation of materials [12,32]. Logically, these strategies aim to regulate the intrinsic properties of interlayer (e.g. conductivity, polarity, catalytic properties, etc.) from the material perspective, thereafter strengthening the interlayer's performance towards blocking and conversion of polysulfides. The question is that Li−S batteries still show capacity fading [33,34], even equipped with a well-designed interlayer with reasonable chemical components and microstructures. This might be related to the limited suppression and conversion efficiency of interlayers to polysulfides, which principally results from the performance ceiling imposed by the inherent properties of the applied materials. Given that, it is paramount to examine supplementary strategies that can maximize the suppression capabilities of the interlayer besides designing or modifying the intrinsic nature of interlayer material for Li−S batteries.

The water filter consists of four media layers (Fig. S1), where each layer performs a specific function in sifting the impurities with different sizes (10−0.0001 μm) in water. By hierarchically arranging the architecture of these layers, the filter enables complete water purification. It is worth mentioning, that the filtration efficiency is supposed to be highly stacking sequence-dependent on these media layers. Swapping their stacking sequence could lead to an incomplete purification of water. Taking inspiration from the water filter, we question whether this principle is suitable for Li−S batteries, and if the stacking configuration of two layers with distinct functions affects the suppression efficiency of polysulfides. In this scenario, a conductive layer prepared from the carbonized polyacrylonitrile-carbon nanotube (CPCNT) and an electrocatalytic layer made from the carbonized polyacrylonitrile-selenium (CPSe) was fabricated via an electrospinning method, as illustrated in Fig. 1a. In our plan, the conductive layer is used to restrain polysulfide shuttling, whilst the catalytic layer will accelerate the conversion kinetics of polysulfides. With swapping their contact priority with the sulfur cathode, the overall suppression efficiency of interlayers to polysulfides has been significantly elevated. Accordingly, the interlayer with the configuration of CPSe@CPCNT|S enables the Li−S batteries to persist more than 500 cycles with a low-capacity decay rate of 0.077% at the current density of 1.0°C. More impressively, Li−S batteries with this optimal interlayer architecture sustain 250 cycles with super high-capacity retention at the current density of 0.2°C, even with the sulfur loading of 6.1 mg/cm^2. Further combination of visualized diffusion experiments with finite element simulations confirm that these two interlayer architectures shape a different digesting model to polysulfides, which is closely related to their distinct diffusion damping and conductive access of electrons for polysulfide suppression and conversion. As such, this study elucidates the relationships between the interlayer's spatial configuration and the electrochemical performance of Li−S batteries, providing a brand-new perspective for designing high-performance interlayers in Li−S batteries, with the potential for application in other metal-sulfur batteries.

2. Results and discussion

As schematically illustrated in Fig. 1a, polyacrylonitrile-carbon nanotube (PAN-CNT) and polyacrylonitrile-selenium (PAN-Se) nanofibers were prepared using electrospinning method, respectively. (Experimental details are shown in Supporting Information). The morphology and structure of the as-prepared two nanofiber-shaped samples were characterized with scanning electron microscopy (SEM) and transmission electron microscopy (TEM) techniques. The SEM images in Fig. 1b and c display a typical three-dimensional nanofiber-mesh structure for PAN-CNT and PAN-Se, with both samples having a fiber diameter of around 100−200 nm. Additionally, Fig. 1b reveals another reticulated framework intertwined between CNT and PAN nanofibers. The high-resolution transmission electron microscopy (HRTEM) image further demonstrates the clear lattice fringe with a spacing of 0.34 nm belonging to the (002) plane of CNT [35,36], confirming the entanglement of CNT and carbonized PAN nanofibers (Fig. S2a). Differently, Fig. 1c shows only PAN-Se nanofiber with a smooth appearance, and the HRTEM image of CPSe in Fig. S2b also indicates an amorphous carbon nature with a non-crystalline lattice pattern. Note that the purpose of an extra CNT is to increase the conductivity of CPCNT, and the added Se element provides CPSe with the catalytic activity to accelerate the conversion of polysulfides [37]. Fig. 1d−e presents HADDF-TEM images, and the corresponding energy dispersive X-ray spectroscopy (EDS) analyses of CPCNT and CPSe, respectively. These images verify the homogenous distribution of C and N in CPCNT (Fig. 1d) and C, Se, and N in CPSe materials (Fig. 1e). The overall X-ray photoelectron microscopy (XPS) spectra also confirm the existence of Se 3D peak in CPSe, while CPCNT only contains C 1s, N 1s, and O 1s peaks (Fig. 1f). These results align with EDS elemental mapping. In addition, the thermal stability of CPCNT and CPSe was assessed with thermogravimetric analysis (TGA) in the N_2 atmosphere at 700 °C. As shown in Fig. 1g, CPCNT retains 83.2% weight even at a high temperature of 700 °C, indicating its high thermal stability. In comparison, CPSe only maintains its 63% weight at the same temperature. The weight loss of CPSe is ascribed to the evaporation of Se and the further cross-linking reaction of partially uncarbonized PAN during preparation [38]. The Se content in CPSe is quantified to be 95.4 g/kg with inductively coupled plasma-mass spectrometry (ICP-MS). Accordingly, the above results sufficiently manifest the interwoven of CNT and the doping of Se in carbonized PAN nanofibers, respectively.

N_2 adsorption/desorption isotherms of CPCNT and CPSe were collected at 77 K. As shown in Fig. S3, both CPCNT and CPSe display type II isotherms with H4 hysteresis loop, indicating a mesoporous architecture with fewer macropores for both samples [39]. The pore size distribution further confirms mesoporous-dominant pore structure for the CPCNT(D_{BJH} = 7.5 nm, where D_{BJH} is pore diameter calculated from Barrett-Joyner-Halenda method) and CPSe (D_{BJH} = 5.8 nm) in the inset of Fig. S3a and b, respectively. This mesopore structure will benefit the penetration of electrolytes and the adsorption of polysulfide [40]. However, CPCNT exhibits a larger Brunauer-Emmett-Teller (BET) surface area (S_{BET}) of 385 m^2/g than CPSe (S_{BET} = 291 m^2/g), implying that CPCNT will provide more space for physically confining polysulfides. The increased specific surface area is closely related to the added CNT in CPCNT and porous structures generated at higher carbonization temperature. The N_2 adsorption-desorption isotherms effectively differentiate the CPCNT and CPSe from its surface areas and porous properties.

The electrochemical performance of Li−S cells assembled with different interlayer configurations (IC) was thoroughly evaluated with 2025-type coin cells. To strictly guarantee the reasonability of experimental design, five interlayer configurations (Table S1) were proposed for electrochemical measurements with Li−S cells, including CPSe@CPCNT|S (IC-1), CPCNT@CPSe|S (IC-2), CPCNT@CPCNT|S (IC-3),

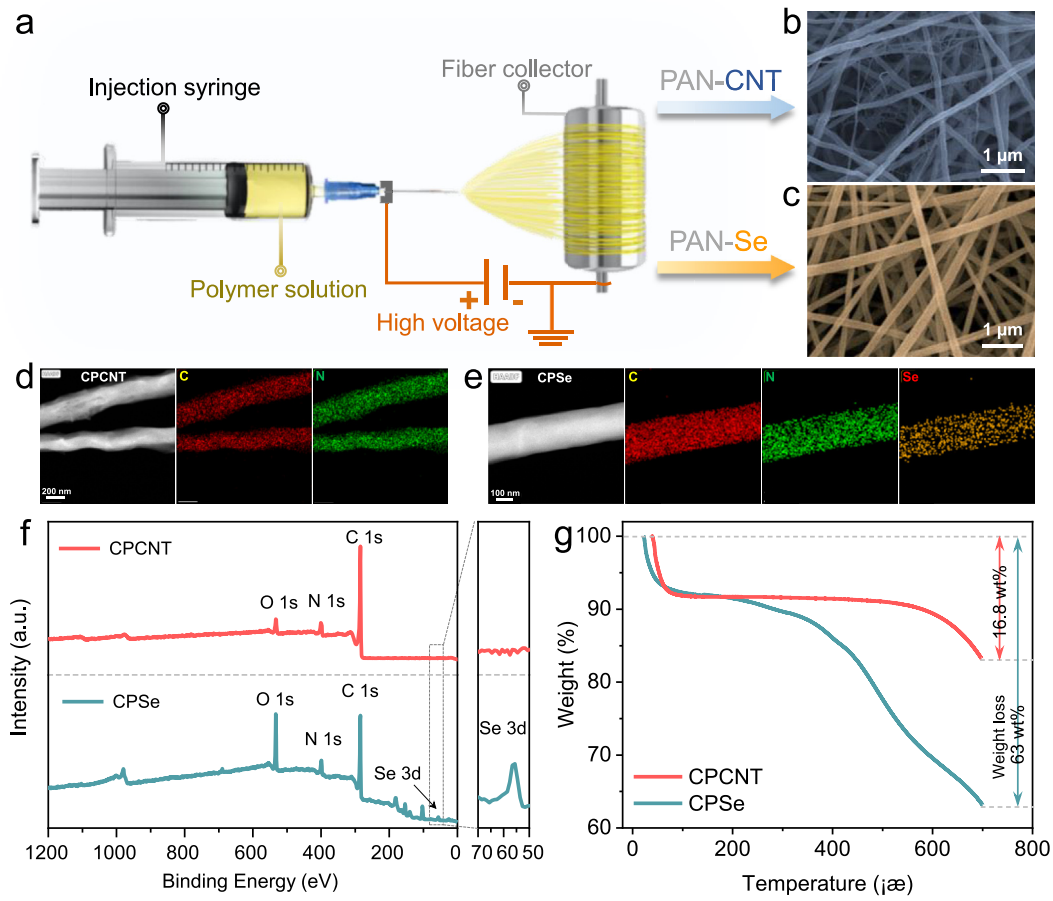

Fig. 1. (a) Schematic illustration of electrospinning for the fabrication of PAN-CNT and PAN-Se fibers. SEM images of as-electrospun (b) PAN-CNT and (c) PAN-Se fibers. High-angle annular dark-field transmission electron microscopy (HAADF-TEM), and the corresponding elemental mapping images of (d) CPCNT and (e) CPSe. (f) Overall XPS analyses of CPCNT and CPSe. (g) TGA curves of CPCNT and CPSe measured in the N_2 atmosphere at 700 °C.

CPSe@CPSe|S (IC-4), CPCNT-Se@CPCNT-Se|S (IC-5). The thickness of CPCNT and CPSe is controlled to be around 52 μm (Fig. S4). Schematically, the Li—S cells planted IC-1 and IC-2 interlayers are illustrated in Fig. 2a. In IC-1, the CPCNT layer is in contact with the sulfur cathode, whereas the CPSe layer is on top of the sulfur cathode in IC-2. Herein, IC-1 and IC-2 are mainly expected to examine the effect of stacking configuration on the suppression efficiency and conversion kinetics of polysulfides. IC-3 and IC-4 are used to exclude the impacts of the increased stacking thickness on the electrochemical performance, whilst IC-5 is fabricated to confirm the necessity of individually preparing conductive and catalytic layers (the functionalities of two layers will be distinguished later). Cyclic voltammetry (CV) curves within the voltage window ranging from 1.8 V to 2.8 V at the sweeping rate of 0.1 mV/s for these specimens are shown in Fig. 2b and Fig. S5a. The CV curves of IC-1 and IC-2 demonstrate the typical redox processes of the sulfur cathode [9,41]. Two cathodic peaks at 2.33 V (peak A) and 2.03 V (peak B) are assigned to the reduction of cyclo-S_8 to the long-chain Li_2S_n ($4 \leq n \leq 8$) and then to insoluble Li_2S_2/Li_2S, respectively. Two anodic peaks at 2.29 V and 2.40 V (peak C) reflect the oxidation of Li_2S/Li_2S_2 to polysulfides and further to S_8. Note that IC-1 reveals a higher current density and smaller polarization potential (ΔE) than that of IC-2, PP (Polypropylene)|S (Fig. 2b), and the reference groups (Fig. S5). Accordingly, these well-designed experiments substantially manifest that the interlayer configurations affect the redox kinetics of Li—S cells. Electrochemical impedance spectroscopy (EIS) measurements were employed to highlight the difference in the charge transfer resistance (R_{ct}) of ICs. Fig. 2c shows the Nyquist plots with the simulated equivalent circuits, in which the depressed semicircle represents R_{ct} at the medium-frequency region. The R_{ct} values of IC-1, IC-2, and PP|S are 31.5, 47.3, and 114.6 Ω, respectively (Table S1). This result indicates that adjusting the stacking configuration of the interlayer is able to effectively reduce the charge transfer resistance, which accounts for the difference in polarization potentials in Fig. 2b. The EIS of IC-3, IC-4, and IC-5 are also compared in Fig. S5, in which the R_{ct} of IC-3 and IC-4 are 26.8 and 63.2 Ω, respectively (Table S1). Thus, IC-1 and IC-3 manifest that the preferential contact of CPCNT with sulfur cathode is conducive to reducing R_{ct}. This phenomenon is attributed to CPCNT as an upper current collector offering additional conductive networks for the redox reaction of active materials [10,42]. In addition, the IC-5 interlayer shows a higher R_{ct} value (52.7 Ω) than that of IC-1 and IC-2, which firmly highlights the advantages of separately fabricating the conductive and catalytic layer and further regulating the stacking structure.

The rate capability and cycling stability of Li—S cells with these interlayers were measured to specify the difference in electrochemical performance. As plotted in Fig. 2d, IC-1 enables Li—S cells to deliver a specific capacity of 1358, 1138, 978, 822, and 674 mAh/g at 0.1, 0.2, 0.5, 1.0, and 2.0C, respectively. The specific capacity returns to 1167 mAh/g when the current density reverts to 0.1C. In contrast, IC-2 and PP|S present evidently lower specific capacities than IC-1 at the corresponding current densities. Interestingly, although IC-3 shows the lowest charge transfer resistance, the specific capacity of Li—S cells with IC-3 is lower than that of IC-1 at the corresponding current density, amounting to only 1214, 1038,

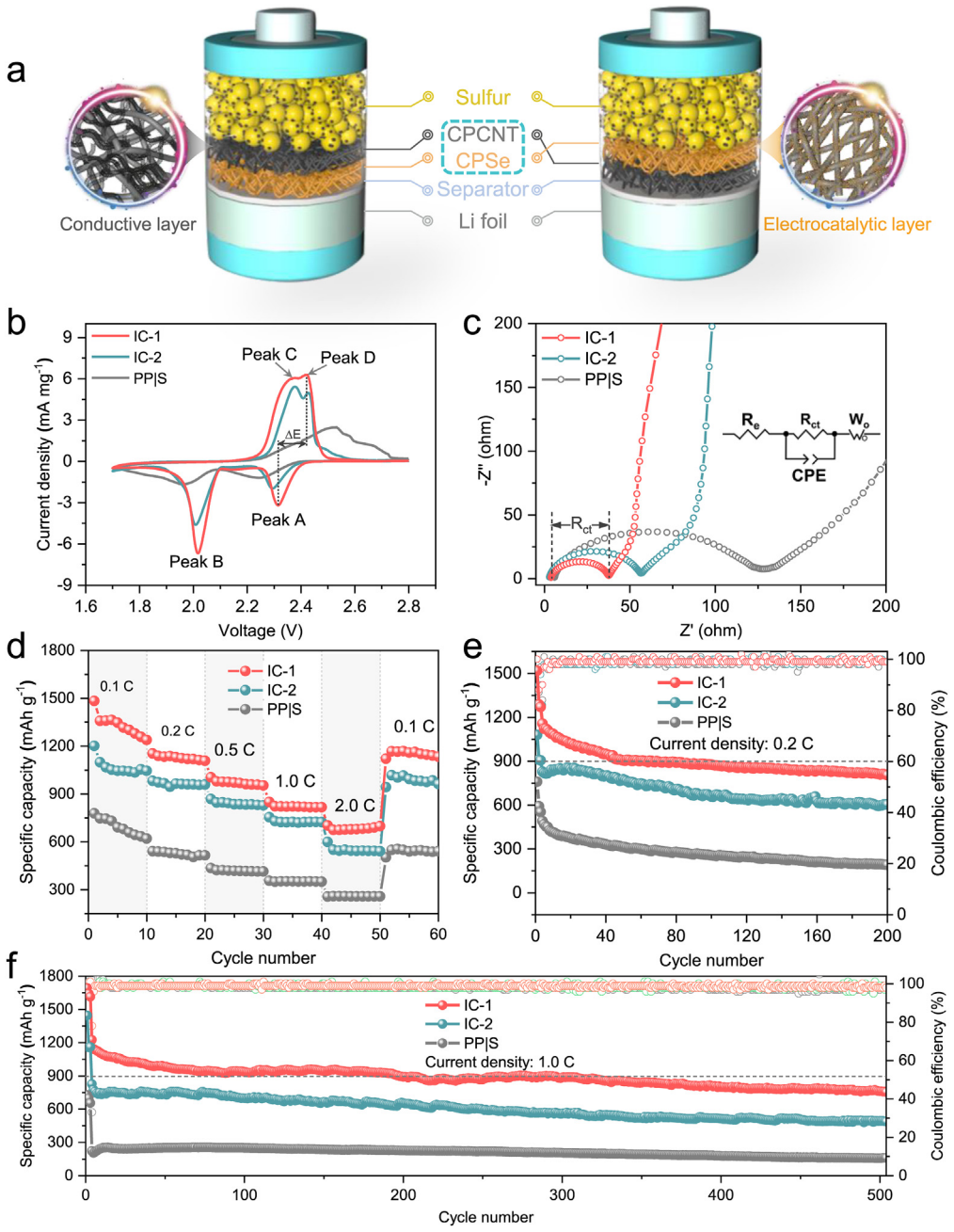

Fig. 2. Electrochemical performance for Li–S cells with different interlayer configurations. (a) Scheme of Li–S cells with IC-1 and IC-2 configurations. (b) CV curves at the first cycle under the scan rate of 0.1 mV/s. (c) Nyquist impedance plots of the fresh Li–S cells. (d) Rate capability at different current densities. (e) Cycling stability and Coulombic efficiency at the current density of 0.2C. (f) Long-term cycling performance with Coulombic efficiency at the current density of 1.0C.

915, 772, and 620 mAh/g (Fig. S6a). Similarly, the rate performance of IC-4 and IC-5 is inferior to IC-1. For a clear comparison, the (dis) charge profiles of all specimens at the current densities of 0.1–2.0C are plotted in Fig. S7. Therefore, the above electrochemical performance validates that leveraging the spatial design of the CPCNT and CPSe can facilitate the redox conversion of polysulfides and lift the sulfur utilization.

The long-term cycling stability of Li–S cells equipped with ICs was also collected at the current density of 0.2 and 1.0C, aiming to evaluate the functional sustainability of the interlayer in polysulfide suppression and conversion. As demonstrated in Fig. 2e, IC-1 allows the Li–S cell to reach a specific capacity of up to 809 mAh/g with almost 100% coulombic efficiency (CE) after 200 cycles at 0.2C. By contrast, the specific capacity of IC-2 is much lower than that of IC-1, maintaining only 603 mAh/g at the 200th cycle. Meanwhile, Li–S cells with IC-3, IC-4, IC-5, and PP also deliver a lower specific capacity than that of IC-1 (Fig. 2e and Fig. S6b), which is 693, 535, 486, and 191 mAh/g at the 200th cycle, respectively. In particular, the specific capacity and CE of each IC and PP at the first three cycles are listed in Table S2. The specific capacity of IC-1 in the initial three cycles is 1157, 1121, and 1123 mAh/g respectively. The specific capacity of IC-1 is consistently higher than IC-2, IC-3, IC-4, IC-5 and PP separator. Meanwhile, the CE of IC-1 approaches 100% at the third cycle, while the rest interlayer configuration remains below 100% even after 3 cycles. Accordingly, the capacity degradation follows the order of PP > IC-5 > IC-4 > IC-2 > IC-3 > IC-1. In this case, it can be deduced (i) the material facing sulfur cathode (i.e.

CPCNT or CPse): will dominantly affect the polysulfide suppression and redox conversion efficiency of the stacked interlayer in Li–S batteries, (ii) solely increasing the stacks or integrating the functionalities of interlayer fail to efficiently improve the electrochemical performance of interlayers in Li–S batteries. All of the corresponding (dis)charge profiles at difference cycles are presented in Fig. S8a, illustrating a typical reduction process ($S_8 \rightarrow Li_2S_8 \rightarrow Li_2S_6 \rightarrow Li_2S_4 \rightarrow Li_2S_2/Li_2S$) and oxidation ($Li_2S_2/Li_2S \rightarrow S_8$) of Li–S batteries [43]. Based on the (dis)charge curves, the polarization potentials (ΔE) at various cycles were also calculated to reflect the improved transformation kinetics of polysulfides by gauging the voltage gap between the oxidation and reduction plateau at 50% capacity. As shown in Fig. S8a, IC-1 features the lowest polarization potential among all samples, which is 165 mV. Clearly, the stacking configurations of CPCNT and CPSe govern ΔE values, perfectly in line with the CV results in Fig. 2a. Meanwhile, the ratio of Q_1 (discharge capacity from S_8 to Li_2S_4) and Q_2 (discharge capacity from Li_2S_4 to Li_2S) at different cycles were further calculated according to Fig. S8a. Ideally, the Q_2/Q_1 ratio is 3. This value roughly quantifies the completion degree of sulfur conversion reaction and the confinement effect on polysulfides [44], which can judge the interlayer's catalytic and inhibition ability to polysulfides. In this work, the Q_2/Q_1 ratio of IC-1 is constantly higher than IC-2 and PP separator, eventually maintaining at 2.4 after the 200th cycle (Fig. S8b). The highest Q_2/Q_1 ratio of IC-1 certifies that the variation of interlayer configuration will regulate the re-utilization efficiency of active materials in Li–S batteries. Additionally, the Q_2/Q_1 ratio of IC-1 superior to IC-3 and IC-4 emphasizes the significance of integrating the interlayer using conductive and catalytic layers, whilst the higher Q_2/Q_1 ratio of IC-1 and IC-2 than IC-5 highlights the necessity of individually fabricating conductive and catalytic layers. The long-term cycling performance for all samples was further compared at a higher current density of 1.0C in Fig. 2f and Fig. S6c, and the related (dis)charge profiles are plotted in Fig. S8c. The cycling stability of IC-1 outperforms the counterparts and PP|S. The specific capacity of IC-1 retains 760 mAh/g even after 500 cycles, which greatly exceeds that of IC-2 (487 mAh/g) and PP|S (160 mAh/g), as well as IC-4 and IC-5 (Fig. S6c). Of note is that although IC-3 possesses the lowest charge transfer resistance, the specific capacity is only 504 mAh/g after 500 cycles. This result emphasizes the importance of incorporating the CPSe layer with catalytic function in the interlayer. Additionally, a performance comparison with the recent reports is provided in Table S3. The optimization of interlayer configuration enables a remarkable improvement in initial capacity and reversible capacity compared with the elaborately designed materials. Fundamentally, the noteworthy improvement in the electrochemical performance of IC-1 elucidates that stacking hierarchical architecture with conductive and catalytic components is an efficient approach to mitigate the capacity degrading and optimize the sulfur utilization of Li–S cells, instead of solely keeping an eye on designing the physical and chemical properties of the electrode materials.

Discerning the role of as-employed CPCNT and CPSe layers towards polysulfides is the precondition to validate this study. For this purpose, CV measurements were initially applied to the symmetric coin cells assembled with CPCNT and CPSe electrodes, respectively. As demonstrated in Fig. S9a, the CV profile contours a pair of broad redox peaks with high-exchange current density for the CPSe electrode, indicating its catalytic characteristics towards Li_2S_6. On the contrary, the redox peak and exchange current density of the CPCNT electrode in Li_2S_6 electrolyte are nearly negligible, suggesting the physical adsorption nature of CPCNT towards Li_2S_6. The specific discharge capacity of IC-1 is also measured to exclude the reactivity of Se with Li^+ when sulfur is removed. As shown in Fig. S10, the specific capacity of IC-1 is less than 3 mAh/g at the current density of 0.2C, which indicates the electrochemical stability of IC-1. Additionally, the visual Li_2S_6 diffusion experiment was also executed in H-type cells separated by the individual CPCNT and CPSe layers. As presented in Fig. S9b, both specimens show transparent solution color in the right vials after 10 min. However, the solution in the right vial with CPSe appears slightly darker yellow compared to the one with CPCNT after 4 h, and this difference becomes more pronounced at 12 h. This observation visualizes a weaker physical confinement capability of CPSe towards polysulfides compared with CPCNT. In principle, this phenomenon can be attributed to their different specific surface area and pore sizes (Fig. S3). Therefore, the properties of CPCNT and CPSe are substantially distinguished, endowing our design concept with logical rationality.

A potentiostatic Li_2S nucleation experiment was conducted to quantify the discrepancy in redox kinetics and conversion efficiency of polysulfides within different interlayer configurations. Fig. 3a describes Li_2S precipitation time and the related deposition capacity in IC-1 and IC-2. The electrochemical transformation of Li_2S in IC-1 reaches the peak value at 839 s, whereas Li_2S nucleation in IC-2 peaks at 2,738 s. Meanwhile, the IC-1 interlayer (157 mAh/g) allows a discharge capacity more than doubled that of IC-2 (76 mAh/g). Quantitatively, the nucleation kinetics of polysulfides is accelerated by more than three-fold, and their conversion efficiency is elevated by 200% in IC-1. The precipitation capacity of IC-1 is also higher than IC-3 (113 mAh/g), IC-4 (66 mAh/g), and IC-5 (57 mAh/g), as shown in Fig. S11. The kinetics is further reflected in the lithium-ion (Li^+) diffusion coefficient (DLi$^+$),and that is calculated from CV profiles at sweeping rates of 0.1–0.5 mV/s in Figs. S12 and S13a–c. All peak current values are linear with the square root of scan rates ($v^{1/2}$) in Figs. S12 and S13d–e, from which the D_{Li}^{+} values are calculated according to the Randles-Sevcik equation [45,46]:

$$I_p = \left(2.69 \times 10^5\right) n^{3/2} A D^{1/2}\ \mathrm{Li}^{+} v^{1/2} C_{\mathrm{Li}^{+}} \quad (1)$$

where, I_p represents the peak current, n is the number of transfer electrons during the redox process ($n = 2$), A is the contact area between S cathode and electrolyte ($A = 0.785\ cm^2$), D Li^+ is the diffusion coefficient of Li^+, v is the scanning rate, DLi$^+$ is the concentration of Li^+ in electrolyte ($C_{Li}^{+} = 1 \times 10^{-3}$ mol/mL). The slopes of each peak in Figs. S12 and S13d–e are positively correlated to the corresponding Li^+ diffusion, where a larger slope is indicative of higher diffusivity. As calculated, the D Li^+ at peaks A, B, and C for IC-1 are 2.099×10^{-7}, 2.532×10^{-7}, and 4.863×10^{-7} cm^2/s, respectively. In contrast, the diffusion kinetics of Li^+ in IC-2, IC-3, IC-4, IC-5, and PP separator is noticeably inferior to IC-1 (Fig. S14 and Table S4). Thus, the facilitated redox kinetics process by IC-1 is synchronized with an enhanced rate capability.

In addition to the kinetics, the diffusion behavior of polysulfides with regards to IC-1 and IC-2 was visualized using the H-type apparatus with 0.2 M Li_2S_6 in dimethoxyethane/dioxolane (DME/DOL) solution to qualitatively examine the blocking ability of interlayers towards polysulfides. As shown in Fig. 3b, the left scheme illustrates the correlated interlayer structure and the right chamber shows the color evolution of the solution at different time nodes. In the initial 10 min, all the right chambers demonstrate a transparent solution. However, the right chamber separated by IC-2 and PP separator clearly presents a light and bright yellow color after 4 h, respectively, and the color of the solution continues to darken after 12 h. Distinct from IC-2 and PP separator, the color of the solution in the chamber divided by IC-1 almost remains colorless until 12 h when it changes to a light-yellow color. The brightness of the solution at the same time nodes intrinsically accounts for the permeation rate of Li_2S_6. This diffusion experiment visualizes the

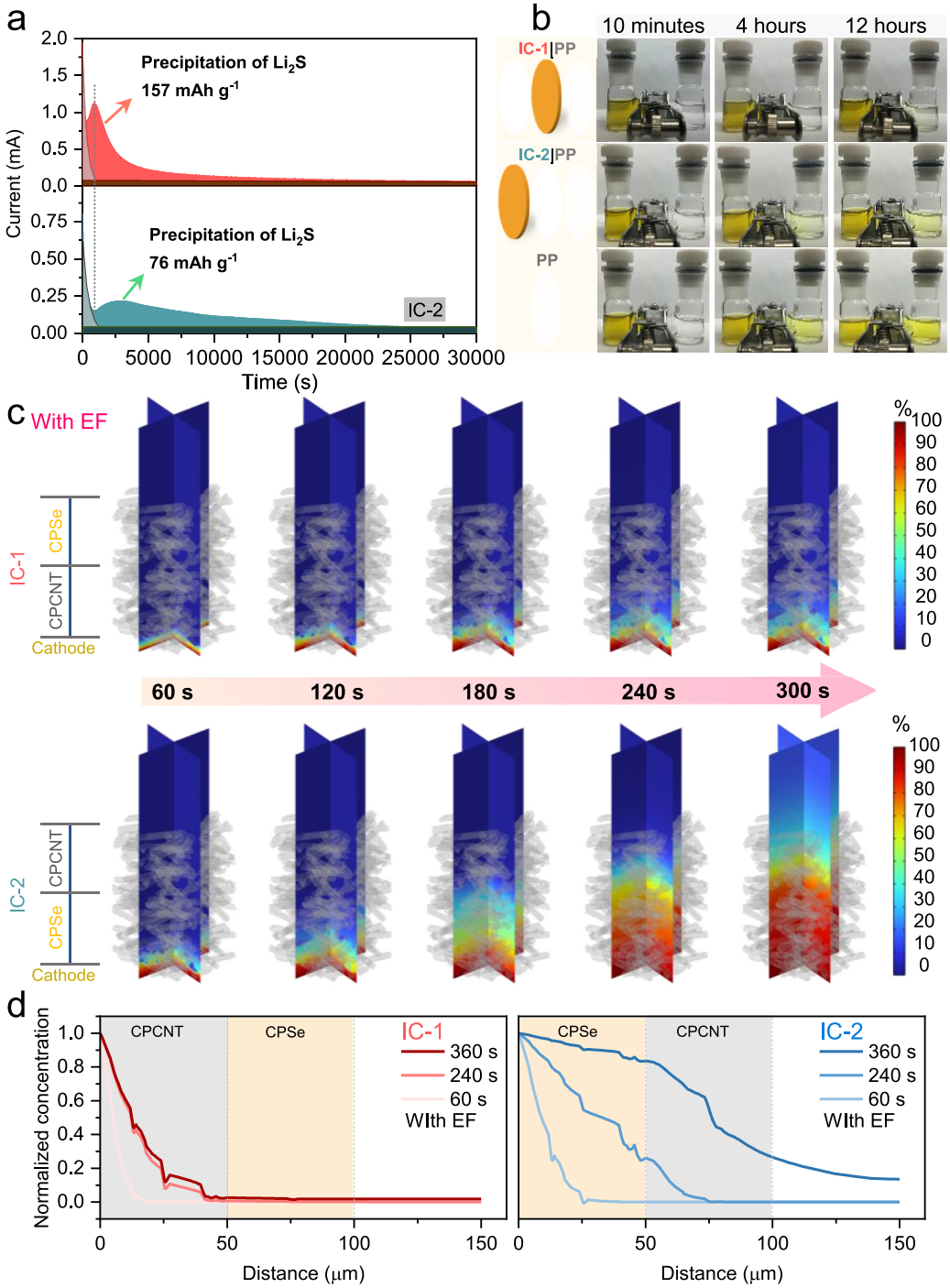

Fig. 3. (a) Potentiostatic discharge curves of Li_2S_8-DOL/DME solution (v:v = 1:1) for IC-1 and IC-2 at 2.05 V and the integral capacity for Li_2S precipitation. (b) Visual measurements of Li_2S_6 diffusion in IC-1, IC-2, and PP separator. (c) 3D COMSOL simulations for Li_2S_6 diffusion process with applied electric field in IC-1 and IC-2. (d) Concentration profile of polysulfides in IC-1 and IC-2 at different time nodes.

strengthened restriction of polysulfides by IC-1, corroborating the effectiveness of our proposed strategy.

Based on the experimental outcomes, a 3D finite elemental analysis (FEA) was executed with COMSOL Multiphysics to simulate the dynamic diffusion process of polysulfides in IC-1 and IC-2 (3D geometric model is shown in Fig. S15, and experimental details are provided in the Supporting Information and Table S5). In the beginning, the simulation proceeded without applying the electric field, to realistically mimic the polysulfide diffusion in two interlayer configurations shown in Fig. 3b. The Li_2S_6 concentration at the surface of the cathode is assumed to be 100% at 0 s (Fig. S16), and the different evolution propensity of color represents the polysulfide concentration. As demonstrated in Fig. S17, IC-1 and IC-2 lead to distinct diffusion behavior. In IC-1, Li_2S_6 is mostly restricted within the CPCNT layer from 60 to 240 s, whereas Li_2S_6 has diffused from CPSe to CPCNT in IC-2 at the same time scale. Interestingly, this result is perfectly consistent with the experimental diffusion behavior shown in Fig. 3b, which can be attributed

to the varied diffusion damping that is determined by the stacking sequence of CPCNT and CPSe. As demonstrated in Fig. S9b, CPCNT features higher diffusion damping to polysulfides than CPSe, which also implies that the Li_2S_6 concentration behind CPCNT in IC-1 is supposed to be lower than that of CPSe in IC-2. As such, the CPCNT layer in IC-1 empowers a significant reduction of Li_2S_6 concentration and forms a lower polysulfide flux behind it, thereby slowing the entire diffusion process together with the following CPSe. On the contrary, IC-2 fails to lower diffusion impetus by effectively decreasing the Li_2S_6 concentration behind the CPCNT layer, hence Li_2S_6 diffuses faster (the detailed mechanism is discussed in Fig. 4). For the first time, the suppression efficiency of polysulfides is reported to be managed by the spatial stacking structure of the interlayer. Herein, Li_2S_6 eventually passes through CPSe of IC-1 and CPCNT of IC-2, and the top region of the model achieves nearly the same concentration after 300 s in Fig. S17. This behavior can be ascribed to the thermal motion of molecules.

Considering that the diffusion of polysulfides in the presence of an electric field might differ from the situation without the electric field, the movement behavior under the action of the electric field was further simulated. Fig. 3c portrays the concentration maps of polysulfides in IC-1 and IC-2 at the time range from 60 to 300 s in the electric field. The diffusion behavior of polysulfides in both working conditions is remarkably different. In terms of IC-1, the dark blue region dominates behind CPSe at 300 s when the electric field is applied to the model (Fig. 3c), while the major color behind CPSe is crystal blue in the absence of an electric field (Fig. S17). This result appropriately indicates a smaller polysulfide migration flux flowing through IC-1 in the electric field, which could benefit from the activated predegrading function of CPCNT as an 'upper current collector' and catalytic conversion of CPSe as the electrocatalyst when the electric field is adopted. More excitingly, the polysulfide shuttle has been significantly suppressed within the IC-1 interlayer even after 300 s. However, IC-2 consents polysulfides to gradually migrate beyond the interlayer from 60 to 240 s and ultimately diffuse to the top boundary at 300 s. The concentration profiles of polysulfide in two interlayer configurations at different time nodes are compared in Fig. 3d. The polysulfide concentration decreases sharply at 60 s in the CPCNT layer of IC-1, in which the attenuation rate is higher than in CPSe of IC-2. Particularly at 180 and 300 s, the polysulfides even diffuse into the CPCNT layer of IC-2 due to the as-developed low diffusion resistance of CPSe to polysulfides, whereas the polysulfides in IC-1 remain in the CPCNT layer of IC-1. These profiles verify that IC-1 will shape a higher diffusion damping to polysulfides and reduce the polysulfide concentration flowing to CPSe for the following electrocatalytic transformation with high efficiency. Therefore, IC-1 generates a more effective hierarchical filter structure, which ensures that the adsorption and conversion efficiency of IC-1 overwhelms that of IC-2.

Accordingly, the suppression mechanism of IC-1 and IC-2 was proposed in Fig. 4, aiming to gain insight into the root cause of such significant differences in the electrochemical behavior of Li–S batteries. As depicted in Fig. 4a, the CPCNT layer is preferentially contacted with the sulfur cathode, followed by the CPSe layer in IC-1. The intimate contact of the CPCNT layer with the sulfur cathode in this model warrants the conductive access for electron transport from the cathode to CPCNT and CPSe, which is confirmed by the overall declined R_{ct} of Li–S cell (Table S1). With this configuration, the CPCNT layer is competent with considerably adsorbing and predegrading polysulfides, shortening the polysulfide chain length (i.e. from S_x^{2-} to S_{x-2}^{2-}/S^{2-} in Fig. 4a), and reducing the polysulfide concentration in the electrolyte during discharge. The CPSe layer will then immediately catalyze the pre-degraded low-concentrated polysulfides (i.e. S_{x-2}^{2-} in Fig. 4a) that diffuse from the CPCNT layer while partially chemisorbing the polysulfides that fail to be converted at the CPCNT layer. However, IC-2 inverts the priority of CPCNT and CPSe, where the CPSe layer is placed on top of the sulfur cathode (Fig. 4b). Unlike CPSe in IC-1, this layer in IC-2 primarily catalyzes the conversion of high-concentrated long-chain polysulfides (i.e. S_x^{2-} in Fig. 4b). This results in comparatively lower electrochemical conversion efficiency, as reflected in the electrochemical Li_2S precipitation of IC-4 (Fig. S11). As a result, the CPSe layer is unable to sharply decrease the concentration of polysulfides. Thereafter, the CPCNT layer will be compelled to trap and degrade high-concentrated polysulfides (i.e. S_x^{2-} in Fig. 4b). Since higher concentration leads to stronger diffusion impetus, and thus

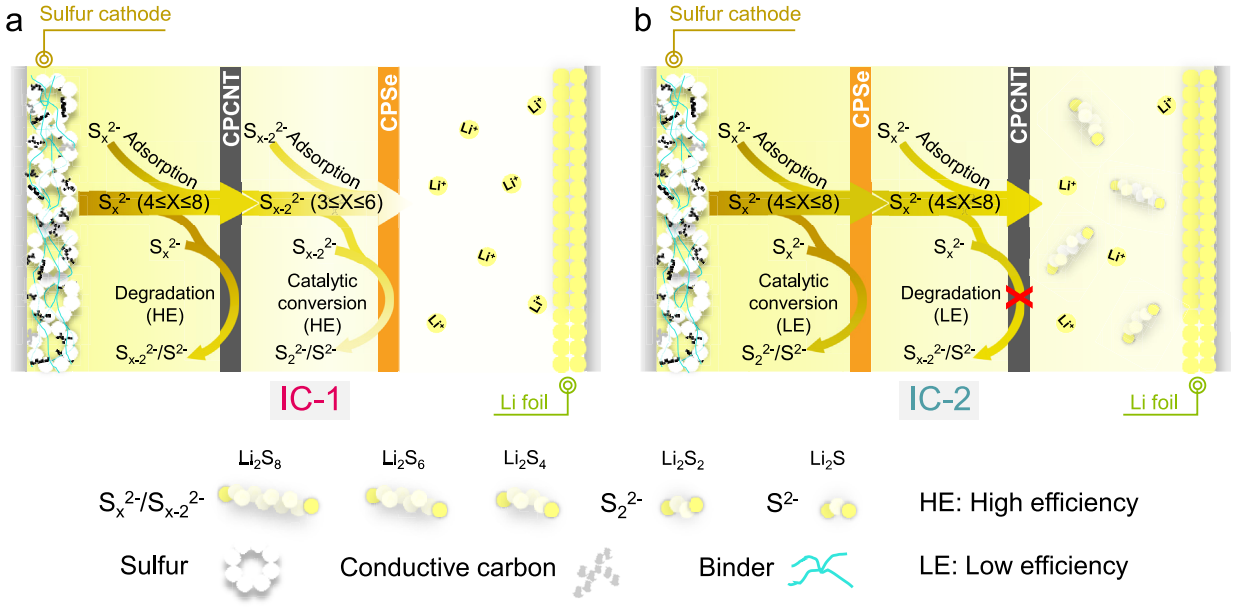

Fig. 4. Schematic illustration of suppression principle for IC-1 and IC-2 during discharge in Li–S batteries.

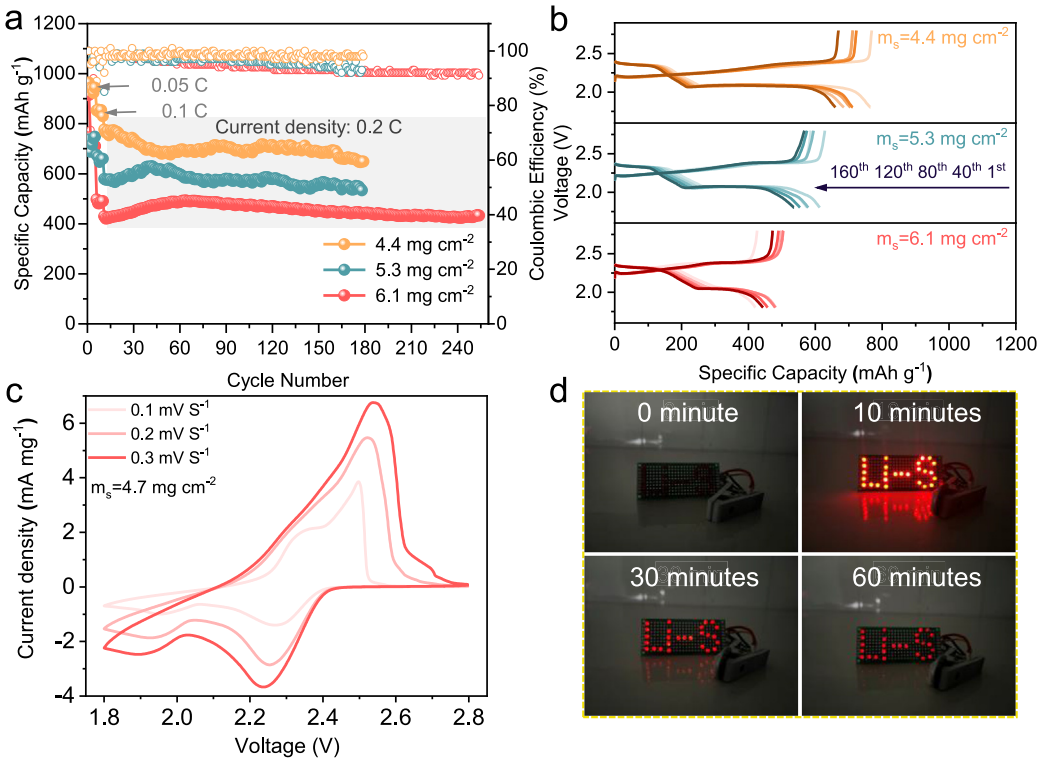

Fig. 5. (a) Long-term cycling stability of Li–S cells with high sulfur loading electrode and (b) the related (dis)charge curves at different cycles. (c) CV profiles of Li–S cells at the scan rate of 0.1, 0.2, and 0.3 mV/s. (d) Digital photograph for Li–S cell continuously lighting LED indicators.

there implies a faster diffusion of polysulfides in electrolyte. Meanwhile, the relatively inferior conductivity of CPSe in IC-2 attenuates the electron motion ability from the sulfur cathode to CPCNT. Hence, increasing the overall charge transfer resistance in the Li–S cell assembled with IC-2 and weakening the electron-accepting pathway of CPCNT for re-utilization of polysulfides. Under this circumstance, the overall suppression competence of IC-2 is comparatively worse than IC-1, leading to a low efficiency for catalytic conversion and degradation of polysulfides, as described in Fig. 4b.

To corroborate the proposed mechanism, the Li content of CPCNT and CPSe for IC-1 and IC-2 at the 20th fully discharged status was precisely quantified with inductively coupled plasma-mass spectrometry (ICP-MS). Herein, the Li content could serve as an indicator indirectly representing the concentration of polysulfides in each interlayer. The Li content in the CPCNT of IC-1 accounts for 2.67 wt% in Table S6, which is evidently higher than in the CPCNT of IC-2 (2.36 wt%). In the meantime, CPSe of IC-1 also demonstrates a slightly higher Li content than that of IC-2. These data reflect their different suppression efficiency of polysulfides caused by interlayer configuration, well consistent with the assumed mechanism. Moreover, the R_{ct} values of Li–S cells planted IC-1 and IC-2 before and after cycling were evaluated using the EIS technique. As plotted in Fig. S18a–c, IC-1 confers Li–S cells to a much smaller $R_{ct,}$ than IC-2 and PP separator at different cycles. Specifically, the R_{ct} of IC-1 drops from 32.5 Ω at fresh status to 11.7 at the 10th cycle and further to 11.1 Ω after 20 cycles with a total reduction amplitude of 21.4 Ω (Fig. S18d). By contrast, the initial R_{ct} of IC-2 is as high as 41 Ω, and its reduction amplitude is only 9.4 Ω after 20 cycles. Even worse, the R_{ct} of reference cells is increased from 114 Ω at the initial status to 116 Ω after the 20th cycle. Such low R_{ct} of IC-1 is conducive to boosting the redox conversion of adsorbed polysulfides upon cycling, efficiently enhancing the sulfur re-utilization. The EIS results also support the assertion of higher efficiency for CPCNT and CPSe in IC-1.

As a proof-of-concept, Li–S cells with high-sulfur loading electrodes were further fabricated to assess the potential of the proposed interlayer for commercial applications. Fig. 5a shows the long-term stability of Li–S cells with IC-1 under the sulfur loading of 4.4, 5.3, and 6.1 mg/cm^2, respectively. The IC-1 interlayer endows all high sulfur loading electrodes with the stable cycling performance at the current density of 0.2C. Specifically, Li–S cell with 4.4 mg/cm^2 sulfur cathode realizes a specific capacity of up to 776 mAh/g and preserves 652 mAh/g with the coulombic efficiency of nearly 100% after 180 cycles. By contrast, Li–S cell with sulfur loading of 4.2 mg/cm^2 delivers much lower capacity when IC-2 is equipped, only maintaining 229 mAh/g after 120 cycles (Fig. S19). Additionally, the 5.3 mg/cm sulfur cathode with IC-1 maintains a capacity of 533 mAh/g after 180 cycles at the current density of 0.2C. More excitingly, the Li–S battery with a sulfur loading of 6.1 mg/cm withstands 250 cycles with a capacity retention of 87%, exceeding the previously reported lifespan [26,32,33,47,48]. The galvanostatic (dis)charge voltage profiles in Fig. 5b also identify the super stable electrochemical behavior of all high-sulfur loading cathode characteristics of two typical (dis) charge plateaus at different cycles. In addition, Li–S cell embedded IC-1 interlayer displays the CV profiles with nearly similar shapes and redox peaks at the sweep rate from 0.1 to 0.3 mV/s, suggesting a decent rate performance even under the sulfur loading of 4.7 mg/cm^2 (Fig. 5c). The as-assembled Li–S cell in Fig. 5d eventually ignites the Li–S pattern consisting of 26 light-emitting diode lamps and endures for more than 60 min, showcasing the promising application of IC-1 in long-lasting Li–S batteries.

3. Conclusions

In summary, we proposed a hierarchical digesting interlayer by engineering the stacking architecture of the interlayer composed of conductive CPCNT and catalytic CPSe nanofibers. This study discloses a spatial factor capable of regulating the efficiency of polysulfide inhibition and sulfur re-utilization in addition to material perspective. Systematic investigations authorize that the IC-1 interlayer with the configuration of CPSe@CPCNT|S forms a more efficient barrier for restricting polysulfide diffusion while remarkably decreasing the charge transfer resistance. Li−S cells paired with IC-1 interlayer ultimately speed up the conversion kinetics and prolong the lifespan, which achieves an outstanding rate performance at different current densities, and a specific capacity of up to 760 mAh/g even after 500 cycles at the current density of 1.0C. Impressively, Li−S cell with a high sulfur loading of 6.1 mg/cm^2 sustains as long as 250 cycles with a capacity retention of 87% at the current density of 0.2C. In-depth experimental analyses and finite elemental simulations expose that IC-1 shapes higher diffusion damping to polysulfides and guarantees the access for electron transport from sulfur cathode to CPCNT and CPSe, which is believed to be the bottom reason leading to significantly enhanced suppression efficiency of polysulfides. This work will enrich the dimensions for designing high-performance interlayers in Li−S batteries and can be extended to other alkali metal-sulfur batteries.

CRediT authorship contribution statement

Wenxi Wang: Writing − review & editing, Writing − original draft, Validation, Project administration, Methodology, Investigation, Funding acquisition, Data curation, Conceptualization. **Lubao Liang:** Writing − original draft, Methodology, Data curation. **Lintong Gao:** Writing − original draft, Methodology, Data curation. **Qi Cao:** Writing − review & editing, Writing − original draft, Validation, Supervision. **Bo Jing:** Writing − review & editing. **Xianyou Wang:** Writing − review & editing. **Hongshuai Hou:** Writing − original draft, Software, Methodology, Data curation. **Wenli Zhang:** Writing − review & editing, Writing − original draft, Validation, Supervision. **Yan Lu:** Writing − review & editing, Writing − original draft, Validation, Supervision.

Declaration of competing interest

The authors declare that they have no known competing financial interests or personal relationships that could have appeared to influence the work reported in this paper.

Data availability

Data will be made available on request.

Acknowledgments

Research reported in this publication was supported by Alexander von Humboldt's research fellowship.

Appendix A. Supplementary data

Supplementary data to this article can be found online at https://doi.org/10.1016/j.mtener.2024.101521.

References

[1] R. Fang, S. Zhao, Z. Sun, D.W. Wang, H.M. Cheng, F. Li, More reliable lithium-sulfur batteries: status, solutions and prospects, Adv. Mater. 29 (48) (2017), https://doi.org/10.1002/adma.201606823.
[2] H. Hao, T. Hutter, B.L. Boyce, J. Watt, P. Liu, D. Mitlin, Review of multifunctional separators: stabilizing the cathode and the anode for alkali (Li, Na, and K) metal-sulfur and selenium batteries, Chem. Rev. 122 (9) (2022) 8053−8125, https://doi.org/10.1021/acs.chemrev.1c00838.
[3] G. Zhou, H. Chen, Y. Cui, Formulating energy density for designing practical lithium-sulfur batteries, Nat. Energy 7 (4) (2022) 312−319, https://doi.org/10.1038/s41560-022-01001-0.
[4] S.F. Ng, M.Y.L. Lau, W.J. Ong, Lithium-sulfur battery cathode design: tailoring metal-based nanostructures for Robust polysulfide adsorption and catalytic conversion, Adv. Mater. 33 (50) (2021) e2008654, https://doi.org/10.1002/adma.202008654.
[5] S. Tu, X. Chen, X. Zhao, M. Cheng, P. Xiong, Y. He, Q. Zhang, Y. Xu, A polysulfide-immobilizing polymer retards the shuttling of polysulfide intermediates in lithium-sulfur batteries, Adv. Mater. 30 (45) (2018) e1804581, https://doi.org/10.1002/adma.201804581.
[6] B. Liu, R. Fang, D. Xie, W. Zhang, H. Huang, Y. Xia, X. Wang, X. Xia, J. Tu, Revisiting scientific issues for industrial applications of lithium-sulfur batteries, Energy Environ. Mater. 1 (4) (2018) 196−208, https://doi.org/10.1002/eem2.12021.
[7] T.Z. Zhuang, J.Q. Huang, H.J. Peng, L.Y. He, X.B. Cheng, C.M. Chen, Q. Zhang, Rational integration of polypropylene/graphene oxide/nafion as ternary-layered separator to retard the shuttle of polysulfides for lithium-sulfur batteries, Small 12 (3) (2016) 381−389, https://doi.org/10.1002/smll.201503133.
[8] Y. Hao, D. Xiong, W. Liu, L. Fan, D. Li, X. Li, Controllably designed 'vice-electrode' interlayers harvesting high performance lithium sulfur batteries, ACS Appl. Mater. Interfaces 9 (46) (2017) 40273−40280, https://doi.org/10.1021/acsami.7b12710.
[9] Y.S. Su, A. Manthiram, Lithium-sulphur batteries with A microporous carbon paper as a bifunctional interlayer, Nat. Commun. 3 (2012) 1166, https://doi.org/10.1038/ncomms2163.
[10] Y.S. Su, A. Manthiram, A new approach to improve cycle performance of rechargeable lithium-sulfur batteries by inserting A free-standing MWCNT interlayer, Chem. Commun. 48 (70) (2012) 8817−8819, https://doi.org/10.1039/c2cc33945e.
[11] S. Zhang, X. Qin, Y. Liu, L. Zhang, D. Liu, Y. Xia, H. Zhu, B. Li, F. Kang, A conductive/ferroelectric hybrid interlayer for highly improved trapping of polysulfides in lithium−sulfur batteries, Adv. Mater. Interfaces 6 (22) (2019) 1900984, https://doi.org/10.1002/admi.201900984.
[12] D. Tian, X. Song, M. Wang, X. Wu, Y. Qiu, B. Guan, X. Xu, L. Fan, N. Zhang, K. Sun, MoN supported on graphene as a bifunctional interlayer for advanced Li-S batteries, Adv. Energy Mater. 9 (46) (2019) 1901940, https://doi.org/10.1002/aenm.201901940.
[13] H. Wu, Y. Huang, S. Xu, W. Zhang, K. Wang, M. Zong, Fabricating three-dimensional hierarchical porous N-doped graphene by a tunable assembly method for interlayer assisted lithium-sulfur batteries, Chem. Eng. J. 327 (2017) 855−867, https://doi.org/10.1016/j.cej.2017.06.164.
[14] D. He, J. Meng, X. Chen, Y. Liao, Z. Cheng, L. Yuan, Z. Li, Y. Huang, Ultrathin conductive interlayer with high-density antisite defects for advanced lithium-sulfur batteries, Adv. Funct. Mater. 31 (2) (2020) 2001201, https://doi.org/10.1002/adfm.202001201.
[15] N. Li, L. Yu, J. Xi, Integrated design of interlayer/current-collector: hetero-nanowires decorated carbon microtube fabric for high-loading and lean-electrolyte lithium-sulfur batteries, Small 17 (37) (2021) e2103001, https://doi.org/10.1002/smll.202103001.
[16] J. Ming, M. Li, P. Kumar, L.J. Li, Multilayer approach for advanced hybrid lithium battery, ACS Nano 10 (6) (2016) 6037−6044, https://doi.org/10.1021/acsnano.6b01626.
[17] M. Li, Y. Wan, J.K. Huang, A.H. Assen, C.-E. Hsiung, H. Jiang, Y. Han, M. Eddaoudi, Z. Lai, J. Ming, L.-J. Li, Metal−organic framework-based separators for enhancing Li−S battery stability: mechanism of mitigating polysulfide diffusion, ACS Energy Lett. 2 (10) (2017) 2362−2367, https://doi.org/10.1021/acsenergylett.7b00692.
[18] G. Ma, F. Huang, Z. Wen, Q. Wang, X. Hong, J. Jin, X. Wu, Enhanced performance of lithium sulfur batteries with conductive polymer modified separators, J. Mater. Chem. A 4 (43) (2016) 16968−16974, https://doi.org/10.1039/c6ta07198h.
[19] L. Fan, M. Li, X. Li, W. Xiao, Z. Chen, J. Lu, Interlayer material selection for lithium-sulfur batteries, Joule 3 (2) (2019) 361−386, https://doi.org/10.1016/j.joule.2019.01.003.
[20] D. Zhu, T. Long, B. Xu, Y. Zhao, H. Hong, R. Liu, F. Meng, J. Liu, Recent advances in interlayer and separator engineering for lithium-sulfur batteries, J. Energy Chem. 57 (2021) 41−60, https://doi.org/10.1016/j.jechem.2020.08.039.
[21] Y.C. Jeong, J.H. Kim, S. Nam, C.R. Park, S.J. Yang, Rational design of nano-structured functional interlayer/separator for advanced Li-S batteries, Adv. Funct. Mater. 28 (38) (2018) 1707411, https://doi.org/10.1002/adfm.201707411.
[22] X. Zhou, Q. Liao, T. Bai, J. Yang, Rational design of graphene @ nitrogen and phosphorous dual-doped porous carbon sandwich-type layer for advanced

lithium-sulfur batteries, J. Mater. Sci. 52 (13) (2017) 7719–7732, https://doi.org/10.1007/s10853-017-1029-2.
[23] K. Yang, L. Zhong, J. Qin, J. Liu, M. Xiao, D. Han, S. Ren, L. Sun, S. Wang, Y. Meng, In situ laminated separator using nitrogen–sulfur co-doped two-dimensional carbon material to anchor polysulfides for high-performance Li–S batteries, ACS Appl. Nano Mater. 1 (8) (2018) 3807–3816, https://doi.org/10.1021/acsanm.8b00557.
[24] J. Park, B.-C. Yu, J.S. Park, J.W. Choi, C. Kim, Y.-E. Sung, J.B. Goodenough, Tungsten disulfide catalysts supported on a carbon cloth interlayer for high performance Li-S battery, Adv. Energy Mater. 7 (11) (2017) 1602567, https://doi.org/10.1002/aenm.201602567.
[25] J. Liu, L. Yuan, K. Yuan, Z. Li, Z. Hao, J. Xiang, Y. Huang, SnO2 as a high-efficiency polysulfide trap in lithium-sulfur batteries, Nanoscale 8 (28) (2016) 13638–13645, https://doi.org/10.1039/c6nr02345b.
[26] M. Geng, H. Yang, C. Shang, The multi-functional effects of CuS as modifier to fabricate efficient interlayer for Li-S batteries, Adv. Sci. 9 (35) (2022) e2204561, https://doi.org/10.1002/advs.202204561.
[27] X. Dai, G. Lv, Z. Wu, X. Wang, Y. Liu, J. Sun, Q. Wang, X. Xiong, Y. Liu, C. Zhang, S. Xin, Y. Chen, T. Zhou, Flexible HieTableTabrarchical Co-doped NiS_2@CNF-CNT electron deficient interlayer with grass-roots structure for Li–S batteries, Adv. Energy Mater. 13 (21) (2023) 2300452, https://doi.org/10.1002/aenm.202300452.
[28] L. Chen, Y. Sun, X. Wei, L. Song, G. Tao, X. Cao, D. Wang, G. Zhou, Y. Song, Dual-functional V_2C MXene assembly in facilitating sulfur evolution kinetics and Li-ion sieving toward practical lithium-sulfur batteries, Adv. Mater. 35 (26) (2023) e2300771, https://doi.org/10.1002/adma.202300771.
[29] C.Y. Fan, S.Y. Liu, H.H. Li, Y.H. Shi, H.C. Wang, H.F. Wang, H.Z. Sun, X.L. Wu, J.P. Zhang, Synergistic mediation of sulfur conversion in lithium-sulfur batteries by a Gerber tree-like interlayer with multiple components, J. Mater. Chem. A 5 (22) (2017) 11255–11262, https://doi.org/10.1039/c7ta02231j.
[30] R. Yi, C. Liu, Y. Zhao, L.J. Hardwick, Y. Li, X. Geng, Q. Zhang, L. Yang, C. Zhao, A light-weight free-standing graphene foam-based interlayer towards improved Li-S cells, Electrochim. Acta 299 (2019) 479–488, https://doi.org/10.1016/j.electacta.2019.01.015.
[31] L. Zhang, X. Chen, F. Wan, Z. Niu, Y. Wang, Q. Zhang, J. Chen, Enhanced electrochemical kinetics and polysulfide traps of indium nitride for highly stable lithium-sulfur batteries, ACS Nano 12 (9) (2018) 9578–9586, https://doi.org/10.1021/acsnano.8b05466.
[32] F. Ma, K. Srinivas, X. Zhang, Z. Zhang, Y. Wu, D. Liu, W. Zhang, Q. Wu, Y. Chen, Mo_2N quantum dots decorated N-doped graphene nanosheets as dual-functional interlayer for dendrite-free and shuttle-free lithium-sulfur batteries, Adv. Funct. Mater. (2022) 2206113, https://doi.org/10.1002/adfm.202206113.
[33] B.J. Lee, C. Zhao, J.H. Yu, T.H. Kang, H.Y. Park, J. Kang, Y. Jung, X. Liu, T. Li, W. Xu, X.B. Zuo, G.L. Xu, K. Amine, J.S. Yu, Development of high-energy non-aqueous lithium-sulfur batteries via redox-active interlayer strategy, Nat. Commun. 13 (1) (2022) 4629, https://doi.org/10.1038/s41467-022-31943-8.
[34] X. Zuo, M. Zhen, D. Liu, H. Yu, X. Feng, W. Zhou, H. Wang, Y. Zhang, A multifunctional catalytic interlayer for propelling solid–solid conversion kinetics of Li_2S_2 to Li_2S in lithium-sulfur batteries, Adv. Funct. Mater. 33 (15) (2023) 2214206, https://doi.org/10.1002/adfm.202214206.
[35] S. Iijima, Helical microtubules of graphitic carbon, Nature 354 (6348) (1991) 56–58, https://doi.org/10.1038/354056a0.
[36] Z. Wang, Y. Yan, Y. Zhang, Y. Chen, X. Peng, X. Wang, W. Zhao, C. Qin, Q. Liu, X. Liu, Single-atomic Co-B_2N_2 sites anchored on carbon nanotube arrays promote lithium polysulfide conversion in lithium-sulfur batteries, Carbon Energy 5 (11) (2023) e306, https://doi.org/10.1002/cey2.306.
[37] W. Wang, K. Xi, B. Li, H. Li, S. Liu, J. Wang, H. Zhao, H. Li, A.M. Abdelkader, X. Gao, G. Li, A sustainable multipurpose separator directed against the shuttle effect of polysulfides for high-performance lithium-sulfur batteries, Adv. Energy Mater. (2022) 2200160, https://doi.org/10.1002/aenm.202200160.
[38] M.S.A. Rahaman, A.F. Ismail, A. Mustafa, A review of heat treatment on polyacrylonitrile fiber, Polym. Degrad. Stab. 92 (8) (2007) 1421–1432, https://doi.org/10.1016/j.polymdegradstab.2007.03.023.
[39] K.S.W. Sing, Reporting physisorption data for gas/solid systems with special reference to the determination of surface area and porosity (recommendations 1984), Pure Appl. Chem. 57 (4) (1985) 603–619, https://doi.org/10.1351/pac198557040603.
[40] J. Balach, T. Jaumann, M. Klose, S. Oswald, J. Eckert, L. Giebeler, Mesoporous carbon interlayers with tailored pore volume as polysulfide reservoir for high-energy lithium-sulfur batteries, J. Phys. Chem. C 119 (9) (2015) 4580–4587, https://doi.org/10.1021/jp512062t.
[41] X. Ji, K.T. Lee, L.F. Nazar, A highly ordered nanostructured carbon-sulphur cathode for lithium-sulphur batteries, Nat. Mater. 8 (6) (2009) 500–506, https://doi.org/10.1038/nmat2460.
[42] Y. Huang, M. Zheng, Z. Lin, B. Zhao, S. Zhang, J. Yang, C. Zhu, H. Zhang, D. Sun, Y. Shi, Flexible cathodes and multifunctional interlayers based on carbonized bacterial cellulose for high-performance lithium-sulfur batteries, J. Mater. Chem. A 3 (20) (2015) 10910–10918, https://doi.org/10.1039/c5ta01515d.
[43] P.G. Bruce, S.A. Freunberger, L.J. Hardwick, J.M. Tarascon, Li-O_2 and Li-S batteries with high energy storage, Nat. Mater. 11 (1) (2011) 19–29, https://doi.org/10.1038/nmat3191.
[44] C. Zhang, B. Fei, D. Yang, H. Zhan, J. Wang, J. Diao, J. Li, G. Henkelman, D. Cai, J.J. Biendicho, J.R. Morante, A. Cabot, Robust lithium-sulfur batteries enabled by highly conductive WSe_2-based superlattices with tunable interlayer space, Adv. Funct. Mater. 32 (24) (2022), https://doi.org/10.1002/adfm.202201322.
[45] X. Tao, J. Wang, C. Liu, H. Wang, H. Yao, G. Zheng, Z.W. Seh, Q. Cai, W. Li, G. Zhou, C. Zu, Y. Cui, Balancing surface adsorption and diffusion of lithium-polysulfides on nonconductive oxides for lithium-sulfur battery design, Nat. Commun. 7 (2016) 11203, https://doi.org/10.1038/ncomms11203.
[46] X.H. Rui, N. Ding, J. Liu, C. Li, C.H. Chen, Analysis of the chemical diffusion coefficient of lithium ions in $Li_3V_2(PO_4)_3$ cathode material, Electrochim. Acta 55 (7) (2010) 2384–2390, https://doi.org/10.1016/j.electacta.2009.11.096.
[47] X. Zhou, J.-L. Yang, N. Li, J. Yang, J. Xi, Highly catalytic porous MoN nanosheets anchored carbon microtubes interlayer for lithium-sulfur batteries, Mater. Today Energy 24 (2022) 100941, https://doi.org/10.1016/j.mtener.2021.100941.
[48] M. Li, H. Chen, C. Guo, S. Qian, H. Li, Z. Wu, C. Xing, P. Xue, S. Zhang, Interfacial engineering on cathode and anode with iminated polyaniline@rGO-CNTs for Robust and high-rate full lithium-sulfur batteries, Adv. Energy Mater. (2023) 2300646, https://doi.org/10.1002/aenm.202300646.